Evaluation of Parametric Assumptions for Shallow Cumulus Convection

A. P. SIEBESMA AND J. W. M. CUIJPERS

Royal Netherlands Meteorological Institute, De Bilt, the Netherlands

(Manuscript received 14 December 1993, in final form 29 June 1994)

ABSTRACT

A large-eddy simulation (LES) model has been utilized to study nonprecipitating shallow convective clouds such as observed during the undisturbed BOMEX period in the trade wind areas. By choosing a realistic large-scale forcing the authors have been able to simulate shallow convective clouds under quasi-steady-state conditions over a long period of 7 hours. This is a necessary condition to investigate diagnostic cumulus parameterization schemes since such schemes usually assume steady-state conditions. The response of the model to the applied large-scale forcing compares well with budget study results of BOMEX. In addition, the LES model delivers detailed information concerning the dynamics of shallow convective clouds. This is used to verify basic parameterizations of turbulent fluxes and entrainment and detrainment rates used in large-scale models. The most important conclusions are (i) the fractional entrainment and detrainment rates used in present large-scale atmospheric models are one order of magnitude too small, confirming previous results obtained by Esbensen, and (ii) estimates of turbulent fluxes by bulk cloud updrafts and environmental downdrafts give an underestimation of 20% to 50% depending on the variable that is transported. Implications of these results for cumulus parameterizations will be discussed.

1. Introduction

Shallow convection by trade wind cumuli in the subtropical belts influences the large-scale atmospheric dynamics significantly. The enhanced vertical convective mixing of heat and moisture due to these clouds increases the surface evaporation, especially above the subtropical oceans. The moisture collected in the trade wind areas is transported downstream to the intertropical convergence zone (ITCZ), where it is finally released as latent heat in deep convective tropical disturbances. Since this latent heat release in the ITCZ is the engine of the Hadley circulation, the surface evaporation upstream in the undisturbed trade wind areas can be regarded as the main fuel supply for this circulation. In this context it is clear that the presence of trade wind cumuli intensifies the large-scale circulation.

Locally, the vertical mixing of heat and moisture by trade wind cumuli is also important to counteract the drying and warming effects of the large-scale subsidence induced by the Hadley circulation. As a result, a quasi-steady thermodynamic state of the cloud and inversion layer in the undisturbed trade wind regions can be maintained.

Most studies of undisturbed trade wind cumuli are based on large-scale budget results obtained from field experiments such as BOMEX (Holland and Rasmusson 1973; Nitta and Esbensen 1974) and ATEX (Augstein et al. 1973). By making various assumptions, numerous diagnostic cloud models, both spectral (Nitta 1975) and bulk (Yanai et al. 1973; Betts 1975; Esbensen 1978; Albrecht et al. 1979; Hanson 1981), have been developed from these large-scale budgets in order to gain more insight into the physical mechanisms. Such conceptual cloud models compute vertical mass fluxes and entrainment and detrainment rates, which cannot be obtained directly from large-scale budgets.

Results of such cloud models can in principle be used to design parameterization schemes for large-scale models. Unfortunately, parameterization of shallow cumulus convection is not well advanced and, in fact, is ignored in most models. Only a few operational schemes exist that treat shallow convection as a part of a more general convection scheme (Tiedtke 1989; Gregory and Rowntree 1990). The first scheme (Tiedtke 1989) is operational in the model of the European Centre for Medium-Range Weather Forecasts (ECMWF) and in the ECHAM model (Roeckner et al. 1992), which is a climate version of the ECMWF model and is developed at the Max Planck Institute in Hamburg. The latter scheme (Gregory and Rowntree 1990) is used in the model of the U.K. Meteorological Office.

The impact of such parameterizations on the large-scale flow has been demonstrated by comparing a 50-day integration of a general circulation model including a shallow convection scheme with an integration with-

Corresponding author address: Dr. Pier Siebesma, KNMI, P.O. Box 201, De Bilt AE 3730, the Netherlands.
E-mail:siebesma@knmi.nl

out such a scheme (Tiedtke et al. 1988). The main results were an increase of the surface evaporation especially above the subtropical oceans by as much as 50 W m^{-2} to more realistic values. Precipitation was enhanced in some areas in the ITCZ by up to 10 mm day^{-1}. The hydrological cycle was intensified and hence also the Hadley circulation, resulting in stronger and more realistic subtropical anticyclones especially over the Atlantic Ocean. From these results we can conclude that it is important to parameterize shallow convection by these cumuli in large-scale models.

The objective of this paper is to investigate the various assumptions that lead to such a parameterization. In particular we will focus on two important issues. First, in many convection schemes, both for shallow and deep convection, turbulent fluxes are estimated using a mass flux approach by only considering major updrafts and compensating subsidence. Recently this approach has been extended to the convective boundary layer (Randall et al. 1992) and the stratus-topped boundary layer (Moeng et al. 1992). It is completely unclear, however, whether and under what conditions such an approach can be made. Second, an important parameter in convection schemes is the fractional entrainment and detrainment rate that dictates the mass exchange between clouds and the environment. Using a bulk cloud model Esbensen (1978) has found fractional entrainment and detrainment rates, derived from the BOMEX large-scale budgets, that appear to be an order of magnitude larger than the rates used in the above-cited parameterization schemes. Clearly, there is a problem here. Either the diagnostic cloud model by Esbensen made wrong assumptions or the referred parameterization schemes use ill-defined physical concepts.

In order to shed some new light on the aforementioned problems and inconsistencies, we will use and promote in this paper the following approach: Using a high-resolution large-eddy simulation (LES) model we will create a simulation that is in agreement with observations from the undisturbed period of phase 3 of the Barbados Oceanographic and Meteorological Experiment (BOMEX). The results of the simulation will then be used to verify the aforementioned assumptions.

In order to make a large-eddy simulation for such a purpose one has to meet two important conditions. First, the size of the computational domain has to be such that it is capable of containing a cloud ensemble large enough to average out the life cycles of the individual clouds. Second, there has to be a realistic large-scale forcing that balances the activity of the cumulus field generated by the LES model. Only if these conditions are met can one use these results to test cumulus parameterization schemes and cloud models since they are formulated (or can perhaps only be formulated) assuming the cloud field to be in equilibrium with its large-scale forcing.

In the past, several large-eddy simulations of shallow convective cases have been reported (Sommeria 1976; Sommeria and Lemone 1978; Beniston and Sommeria 1981; Bougeault 1981; Nicholls et al. 1982; and Cuijpers and Duynkerke 1993). None of these studies, however, did produce a satisfactory steady state. Especially the humidity fields of all the above-quoted simulations did show large drift terms ranging from 4 to 10 g kg^{-1} day^{-1}. In the present case we will put special emphasis on achieving a quasi-steady state.

In section 2 we will give a short description of the LES model we have used for the simulations. The description of the initial conditions and the applied large-scale forcing to the model inspired from the BOMEX data will be given in section 3. We will compare and discuss the response of the LES model to this forcing with the large-scale budgets from BOMEX in the same section. Having gained faith in the model results the heart of the matter will be presented in section 4 and 5. In section 4 we will compare several turbulent flux approximations made in the various cloud models and parameterization schemes with the LES model results and in section 5 discuss how the entrainment and detrainment rates can be determined from the LES model results. The rates computed by the model will be interpreted and compared with the rates used in cloud models and parameterization schemes operational in the present general circulation models. Conclusions and perspectives for the parametric description of shallow convection in large-scale models will be given in section 6.

2. Description of the LES model

The resolution of a large-eddy simulation (LES) model is such that the largest eddies of a three-dimensional turbulent field are resolved. As a result the bulk of the turbulent field can be explicitly resolved by the model and the smaller subgrid eddies can be parameterized realistically due to the well-known scaling behavior in the inertial subrange. For a detailed description of the LES model the reader is referred to Cuijpers and Duynkerke (1993). Here it will suffice to recall the main characteristics.

The set of prognostic equations, which is the usual set of meteorological equations for moist air within the Boussinesq approximation, is solved at each grid point inside a computational domain of 5 × 5 km^2 in the horizontal and 4 km in the vertical. These variables are the u, v, and w components of the velocity field, the liquid water potential temperature θ_l, and the total water specific humidity q_t. These last two variables are defined as

$$\theta_l = \theta - \frac{L}{c_p}\frac{\theta}{T} q_l \equiv \theta - \frac{L}{c_p \pi} q_l$$

$$q_t = q_v + q_l, \tag{2.1}$$

where L is the latent heat of vaporization, c_p the specific heat of dry air at constant pressure, θ the potential temperature, T the absolute temperature, q_v the specific humidity for water vapor, and q_l the specific humidity for liquid water. We also introduced the Exner function π, the ratio of absolute and potential temperature. If there is no ice or precipitation, θ_l and q_t are conserved for moist-adiabatic processes. Therefore, condensation processes do not enter in the prognostic equations.

Subgrid-scale turbulent fluxes are determined using a $1\frac{1}{2}$-order closure scheme (Deardorff 1973), for which an additional prognostic equation of the turbulent kinetic energy is solved. The local pressure fluctuations are calculated from a Poisson equation, while the horizontal slab–averaged pressure is updated diagnostically assuming hydrostatic equilibrium. Condensation effects are determined using a simple all-or-nothing scheme. The surface temperature and specific humidity are prescribed and the resulting surface fluxes are derived from the Monin–Obukhov similarity theory using the usual flux gradient relations (Dyer 1974). At the model top there is a sponge layer that removes fluctuations of the velocity, temperature, and humidity fields. The lateral boundary conditions are cyclic.

The domain is divided in $40 \times 40 \times 100$ grid boxes with a horizontal dimension of 125×125 m^2 and a vertical dimension of 40 m. The time step for integration is 4 seconds. We have, however, also performed calculations using different domain sizes in order to investigate finite size effects (see below). Since we will be mainly interested in the dynamics of the horizontal slab–averaged fields we will focus here on the tendency equations of these slab-averaged fields. In general one can split these tendency equations into two parts: 1) a part calculated by the LES model resulting from the scales smaller than the size of the computational domain, and 2) a large-scale forcing part that needs to be prescribed resulting from scales larger than the domain size of the model. Schematically this can be written as

$$\frac{\partial \overline{\chi}}{\partial t} = \left(\frac{\partial \overline{\chi}}{\partial t}\right)_{\text{model}} + \left(\frac{\partial \overline{\chi}}{\partial t}\right)_{\text{forcing}}, \qquad (2.2)$$

with $\chi = u, v, \theta_l$, or q_t, and overbars denoting a slab average over the horizontal domain of the model. The first term, the model tendency of χ averaged over the horizontal domain, is just the turbulent flux divergence as calculated by the LES model

$$\left(\frac{\partial \overline{\chi}}{\partial t}\right)_{\text{model}} = -\frac{1}{\rho}\left(\frac{\partial \rho \overline{w'\chi'}}{\partial z}\right), \qquad (2.3)$$

where ρ is the slab-averaged density and the prime denotes deviations from the horizontal slab average. The forcing term on the right-hand side of (2.2) takes the following form for the various prognostic variables (Sommeria 1976):

$$\begin{aligned}
\left(\frac{\partial \overline{u}}{\partial t}\right)_{\text{forcing}} &= -\overline{u}\frac{\partial \overline{u}}{\partial x} - \overline{v}\frac{\partial \overline{u}}{\partial y} - \overline{w}\frac{\partial \rho \overline{u}}{\rho \partial z} + f(\overline{v} - v_g) \\
\left(\frac{\partial \overline{v}}{\partial t}\right)_{\text{forcing}} &= -\overline{u}\frac{\partial \overline{v}}{\partial x} - \overline{v}\frac{\partial \overline{v}}{\partial y} - \overline{w}\frac{\partial \rho \overline{v}}{\rho \partial z} - f(\overline{u} - u_g) \\
\left(\frac{\partial \overline{\theta_l}}{\partial t}\right)_{\text{forcing}} &= -\overline{u}\frac{\partial \overline{\theta_l}}{\partial x} - \overline{v}\frac{\partial \overline{\theta_l}}{\partial y} - \overline{w}\frac{\partial \rho \overline{\theta_l}}{\rho \partial z} + \left(\frac{\partial \overline{\theta_l}}{\partial t}\right)_{\text{Rad}} \\
\left(\frac{\partial \overline{q_t}}{\partial t}\right)_{\text{forcing}} &= -\overline{u}\frac{\partial \overline{q_t}}{\partial x} - \overline{v}\frac{\partial \overline{q_t}}{\partial y} - \overline{w}\frac{\partial \rho \overline{q_t}}{\rho \partial z}, \qquad (2.4)
\end{aligned}$$

where f is the Coriolis parameter and u_g and v_g are prescribed components of the geostrophic wind. Since we want to keep the prescribed large-scale subsidence constant with time the large-scale forcing tendency of $\overline{w}$ is kept zero.

The large-scale averages $\overline{u}$ and $\overline{v}$ and the vertical derivatives of $\overline{u}$, $\overline{v}$, $\overline{\theta_l}$, and $\overline{q_t}$ appearing on the right-hand side of (2.4) can be updated from the LES model as, respectively, horizontal slab averages and vertical derivatives from these slab averages. The horizontal large-scale gradients appearing in (2.4) cannot be calculated by the LES model and need to be prescribed. They only appear in the large-scale forcing and are not absorbed in the actual fields since the large-scale gradients hardly affect the fields on a domain size of 5 km. Finally, in the tendency equation of θ_l a term for the radiative flux divergence has been included. In the present simulation we have prescribed the radiative flux divergence rather than using a time consuming radiation scheme. The justification of this simplification for cases with a low cloud cover of 0%–20% has been demonstrated by Cuijpers (1994). If the large-scale forcing is chosen realistically, there will be a balance between this forcing and the turbulent field generated by the LES model. As a result a stationary state will evolve naturally.

3. Case description and general characteristics of the simulation

a. Description of the case

Our goal in this section is to create a simulation that is in agreement with observations and that is in an acceptable steady state so that cumulus parameterization assumptions can be verified. During phase 3 of BOMEX from 22 to 30 June 1969 a detailed observational budget study in a 500×500 km^2 square near Barbados has been performed. Data were obtained from rawinsondes launched every $1\frac{1}{2}$ h from four ships located at the corners of the BOMEX array. From these data large-scale heat and moisture budgets have been deduced (Holland and Rasmusson 1973; Nitta and Esbensen 1974). For the purpose of our simulation, we will concentrate on the undisturbed BOMEX period of

phase 3 from 22 to 26 June during which nonprecipitating cumuli were the only type of cumulus convection that was observed.

Ideally, we would like to initialize the LES model with the average observed profiles of u, v, θ_l, and q_t of this 5-day period and run the model using the diagnosed large-scale forcing. This is, however, not feasible since the temporal and spatial variations of the fields are such that an actual inversion, such as appears on most individual soundings, is not found in the mean soundings (Nitta and Esbensen 1974). Therefore, instead, we have selected from the *BOMEX Rawinsonde Atlas* (BOMEX Center for Experiment Design and Data Analysis 1975a) a mean profile of one individual ship over a shorter period. We used the mean profile of the NOAA Ship *Oceanographer,* the most northern ship of the BOMEX square, averaged over 22 and 23 June, during which a well-defined steady state with a strong inversion was present. For the large-scale forcing we use the diagnosed forcing for the whole BOMEX square during the undisturbed period.

Figure 1a shows the initial mean vertical profiles of θ and q_v used to start the model. From these initial profiles three distinct layers can be observed. Up to 540 m there is a well-mixed layer with a constant liquid water potential temperature $\theta = 298.7$ K. The total specific humidity q_v is 17.0 g kg^{-1} at 60 m and is slightly decreasing with height. The mixed layer is followed by a conditionally unstable layer where the clouds are formed that extends up to 1500 m. In this layer θ is increasing with height with 3.9 K km^{-1}, and q_v is decreasing with 5.8×10^{-6} m^{-1}. On top of the cloud layer there is an absolutely stable inversion layer in which θ increases strongly with height (11.0 K km^{-1}) and q_v decreases strongly with height (-12.5×10^{-6} m^{-1}). Finally, the layer above the inversion where no clouds are present anymore is relatively unimportant from the meteorological point of view. It is mainly meant to create an absorbing sponge layer that prevents the model from creating unwanted reflections against the top of the model. In the same figure we show the mean rawinsonde measurements of the *Oceanographer* averaged over 22 and 23 June. The error bars denote the typical fluctuations in z direction of q_v and θ during this two-day period.

The initial velocity profiles are shown in Fig. 1b. Since the wind conditions were rather variable, especially above the mixed layer, we do not show wind observations. In the mixed layer the observed wind was on the average 9 m s^{-1} directed mainly westward. Above the mixed layer the wind is assumed to be equal to the geostrophic wind.

From the BOMEX low level atlas (BOMEX Center for Experiment Design and Data Analysis 1975b) the

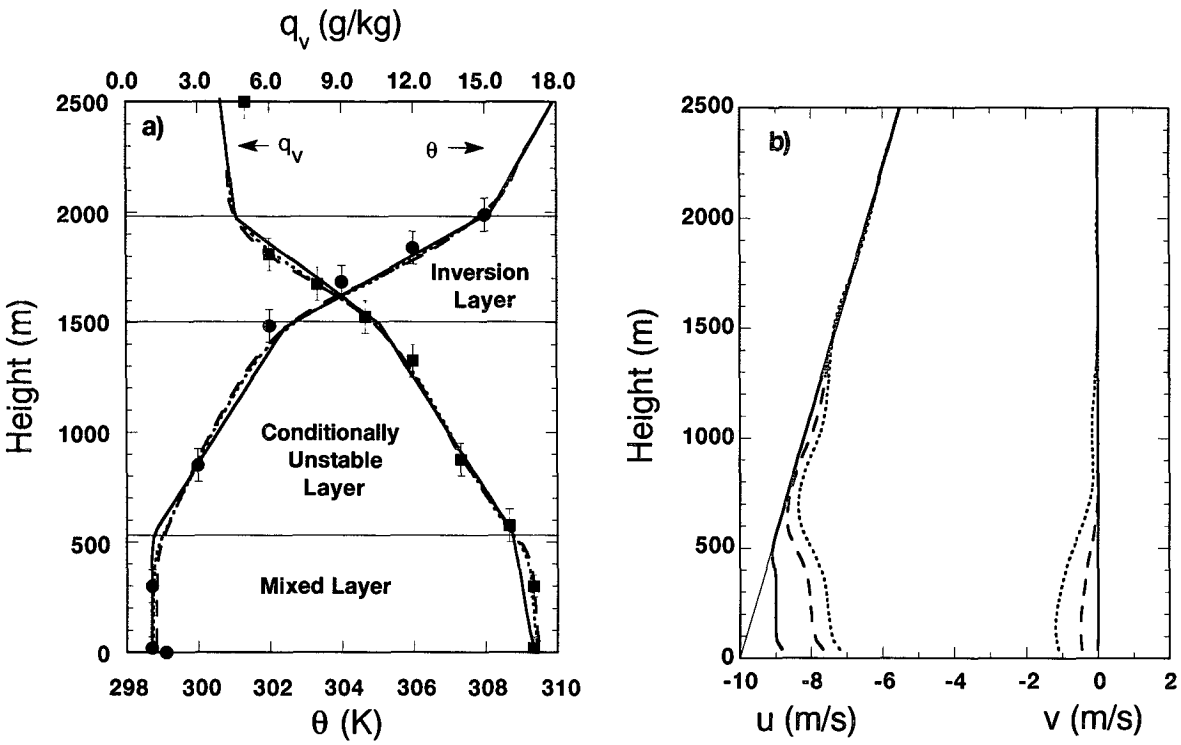

FIG. 1. Horizontally averaged vertical profiles of θ and q_v (a) and the u and v components of the velocity (b) at time $t = 0$ h (full lines), $t = 3$ h (dotted lines), and $t = 7$ h (dashed lines). The circles and squares are the observed values. The thin line in (b) is the prescribed geostrophic wind profile.

oceanic surface values can be found. The surface pressure was 1015 mb, and seawater temperature 300.4 K (corresponding to a θ of 299.1 K). For the surface specific humidity we used the saturation value at the surface temperature, which yields 22.45 g kg^{-1}.

Our choice of the large-scale forcing is dictated by two conditions. First, we want to choose the forcing as simply as possible in order to keep the case transparent. Second, the forcing has to be realistic, that is, in agreement with the diagnosed forcing. In Fig. 2 we show the profiles of the two most important forcing terms, that is, the subsidence $\bar{w}$ and the radiative cooling. These profiles are close to the ones presented by Holland and Rasmusson (1973) and Nitta and Esbensen (1974) for the whole BOMEX square during phase 3. Above the highest cloud tops, that is, above 2000 m where the turbulence is not so active anymore, we want to have a net zero forcing. In order to do so, we have chosen the radiative cooling above 2000 m to be equal to the heating due to subsidence, so that indeed the total heating rate due to the large-scale forcing is guaranteed to be zero.

Another important forcing is the geostrophic wind that is indicated in Fig. 1b. The u component is decreasing with 1.8×10^{-3} s^{-1} corresponding with the observed wind above the mixed layer. This implies a meridional large-scale gradient of the temperature of 2×10^{-3} K km^{-1}, which is approximately the climatological large-scale north–south temperature gradient (Peixoto and Oort 1992). The geostrophic v component of the wind is assumed to be zero.

The final forcing that needs to be prescribed is the large-scale advection. In order to do so we have to specify all the large-scale meridional and zonal gradients of the fields as given by (2.4). Since there is hardly any meridional wind we can safely put all the meridional gradients (i.e., y derivatives) to zero. We also put the zonal large-scale gradients (i.e., the x derivatives) of θ_l and v to zero because no significant advective tendencies of these variables were diagnosed from the observations. Holland and Rasmusson (1973) have diagnosed a low-level drying of about 1 g kg^{-1} day^{-1} due to advection of moisture. Therefore, we have chosen a large-scale zonal gradient of q_l as indicated in Fig. 2 that gives approximately the observed diagnosed drying in the low levels. Finally, the large-scale zonal gradient of u is determined from the large-scale subsidence profile using the continuity equation.

b. Mean statistics and general results

Using the large-scale forcing and initial profiles described in the last paragraph, we have performed a large-eddy simulation of 7 hours. After about 3 hours, the cloud field is well developed and in equilibrium with the large-scale forcing. Figures 1a and 1b show in addition to the initial profiles also the mean profiles of q_v, θ, u, and v after 3 and 7 h. From these figures it is already clear that the fields of thermodynamical interest, that is, the temperature and specific humidity field, are in a steady state. More information, however, can be obtained by looking at the various contributions to the tendencies of these fields over the last 4 h of the simulation. Since we are interested in condensational effects as well, we consider the horizontally averaged prognostic equations of q_v, q_l, and θ:

$$\frac{\partial \bar{\theta}}{\partial t} = -\frac{\partial \rho \overline{w'\theta'}}{\rho \partial z} + \frac{L}{\pi c_p}(c - e) + \left(\frac{\partial \bar{\theta}}{\partial t}\right)_{\text{forcing}}$$

$$\frac{\partial \overline{q_v}}{\partial t} = -\frac{\partial \rho \overline{w'q_v'}}{\rho \partial z} - (c - e) - \left(\frac{\partial \overline{q_v}}{\partial t}\right)_{\text{forcing}}$$

$$\frac{\partial \overline{q_l}}{\partial t} = -\frac{\partial \rho \overline{w'q_l'}}{\rho \partial z} + (c - e) - \left(\frac{\partial \overline{q_l}}{\partial t}\right)_{\text{forcing}}, \qquad (3.1)$$

where c and e are the horizontally averaged condensation and evaporation rates, respectively, as diagnosed by the model. All the terms in (3.1) are averaged over the last 4 hours and are shown in Figs. 3a–c. In the mixed layer, the turbulent flux divergence of q_v is in equilibrium with the large-scale advection while the turbulent flux divergence of θ is almost compensated by the radiative cooling, resulting in a small heating rate of 0.5 K day^{-1}. At cloud base, around 600 m, there are strong condensational effects. These effects are balanced by mainly turbulent mixing processes. The generated heat and liquid water is trans-

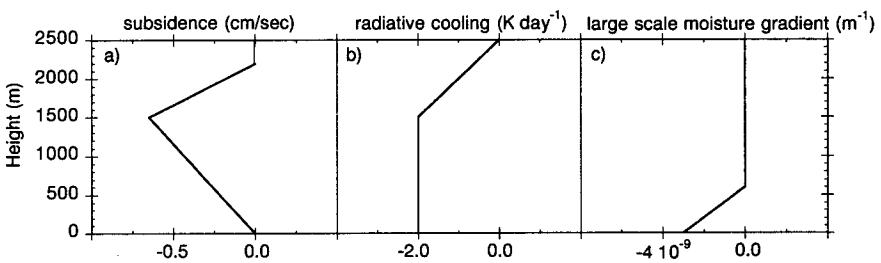

FIG. 2. Profiles of the main components of the large-scale forcing: (a) the large-scale vertical velocity, (b) the radiative cooling, and (c) the large-scale zonal gradient of the specific humidity q_v.

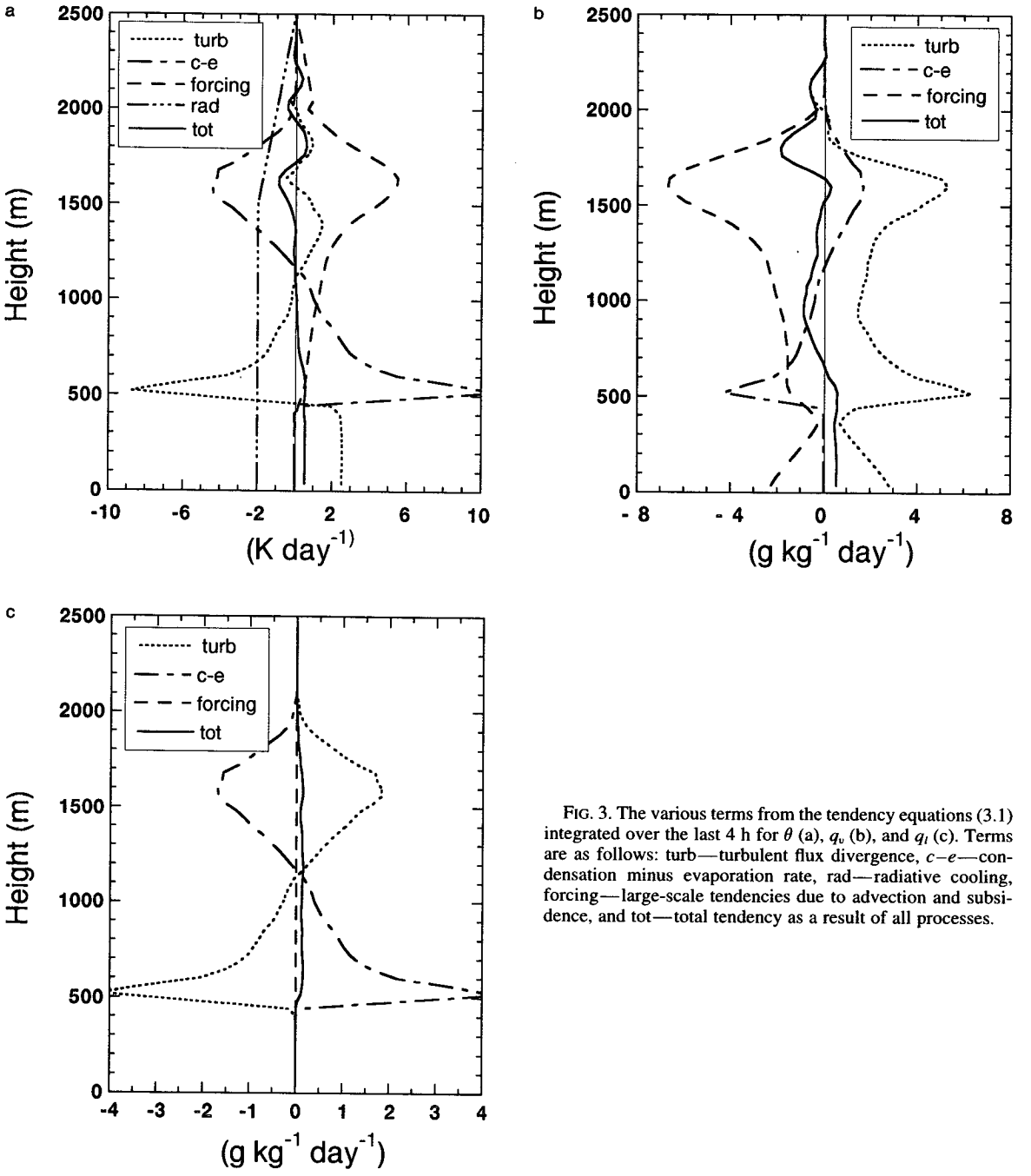

FIG. 3. The various terms from the tendency equations (3.1) integrated over the last 4 h for θ (a), q_v (b), and q_l (c). Terms are as follows: turb—turbulent flux divergence, $c-e$—condensation minus evaporation rate, rad—radiative cooling, forcing—large-scale tendencies due to advection and subsidence, and tot—total tendency as a result of all processes.

ported upward through the clouds. The condensational loss of water vapor is compensated by a net transport of water vapor from the mixed layer below. The liquid water is transported through the clouds until it loses buoyancy in the inversion layer between 1500 and 2000 m, where it evaporates. As a result we can observe strong evaporative cooling and moistening at these levels. The evaporative cooling is compensated by heating due to the large-scale subsidence. For the specific humidity there is a balance in the inversion layer between evaporative moistening, upward turbulent transport of moisture, and drying because of large-scale subsidence.

An important conclusion we can draw from these budgets is that we have succeeded in obtaining a satisfactory steady state since the storage term of θ, q_v, and q_l, that is, the left-hand side of (3.1), is small compared with the various terms of the right-hand side of (3.1). In order to compare the LES results with the observations we show in Fig. 4 the apparent heat source

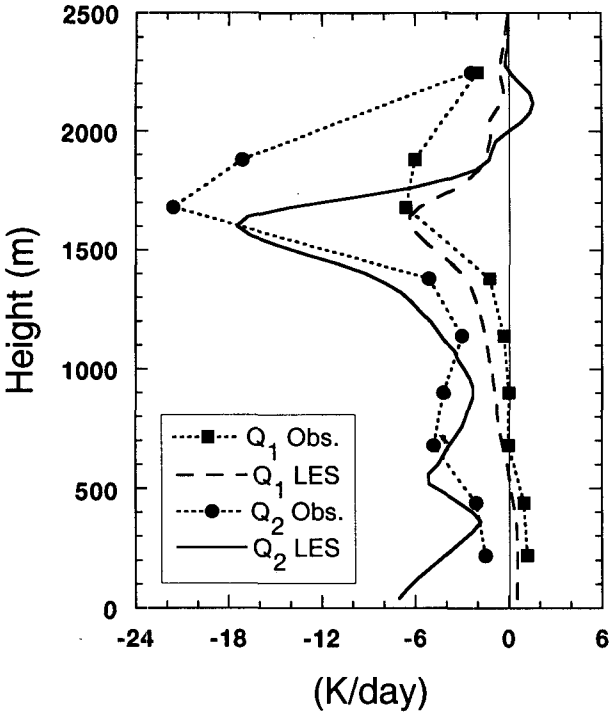

FIG. 4. Apparent heat source Q_1 and apparent moist sink Q_2 calculated from the LES model and compared with BOMEX data as diagnosed by Nitta and Esbensen (1974) on 22–23 June.

Q_1 and the apparent moisture sink Q_2 diagnosed by Nitta and Esbensen (1974) for the whole BOMEX square during 22–23 June together with the LES results. The apparent heat source Q_1 is defined as the sum of the first two terms on the right-hand side of the temperature equation in (3.1) plus the radiative cooling. The apparent moisture sink Q_2 is defined as minus the sum of the first two terms of the right-hand side of the moisture equation (3.1). These terms are (aside from the radiative cooling) just the contributions as determined by the large-eddy model. The agreement between LES model results and the BOMEX data is satisfying. There is only a significant difference in the inversion layer. This is probably due to the fact that the initial profile of the model has been based on data of only one corner of the BOMEX square. The inversion at this corner was somewhat stronger than the inversion obtained by averaging over all soundings in the 500 km × 500 km BOMEX square. As a result it is not surprising that the response Q_1 and Q_2 calculated by the model appears to be less than the diagnosed values based on observations in the whole BOMEX square.

As a further check of the simulation we compared the surface fluxes of the model with the observations. From the model we found that the latent heat flux averaged over the last 4 hours is 150 W m^{-2}. This has to be compared with the observational diagnosed latent heat flux of 170 ± 25 W m^{-2} (Holland 1972) that is estimated as a budget residue for the whole BOMEX square. Measurements of the surface fluxes based on an upper-ocean heat budget analysis for the individual ships suggest that the fluxes diagnosed by the ships on the northern part of the square are 10% lower than the domain-averaged fluxes. Since the model is initialized using surface data of the most northern ship of the square, this might explain the slight underestimation of the fluxes as produced by the LES model.

The sensible heat flux was difficult to determine from an atmospheric budget analysis since it is a small residual of large terms. Various different direct measurements, however, suggest a rather constant Bowen ratio for the BOMEX square ranging between 0.07 and 0.14. This suggests a sensible heat flux of 17 ± 6 W m^{-2}. The model gives a much lower value of 4 W m^{-2}, suggesting a Bowen ratio of 0.025. This discrepancy is probably due to the flux gradient method as suggested by Dyer (1974) used in the LES model. Paulson et al. (1972) compared estimated sensible and latent heat fluxes using the flux gradient method during the BOMEX period with direct eddy correlation measurements. While a good agreement for the latent heat fluxes was obtained, the flux-gradient method underestimated the sensible heat flux by a factor of 2. This explains partly the underestimation of the sensible heat flux in LES model. Fortunately, since the buoyancy flux in the boundary layer is dominated by the latent heat flux, this is not a serious discrepancy for the present analyses.

Finally, we have investigated the model sensitivity to its domain size. We have made simulations on a 2.5 × 2.5 km^2, a 5 × 5 km^2, and a 10 × 10 km^2 computational domain. The time-integrated tendencies of the variables were rather insensitive to the size of the domain. The temporal fluctuations of cloud-related quantities such as cloud cover and liquid water, however, decrease considerably by going from a 2.5 to a 5 km domain. A further increase of the domain size hardly affected the amplitude of the fluctuations. As an example we show in Fig. 5 the total cloud cover, defined as the fractional area covered when all clouds are projected vertically on the bottom of the model, as a function of time for a domain 2.5 km and 5 km. As already discussed in Cuijpers and Duynkerke (1993) these large fluctuations of the cloud cover in the small domain are probably due to the fact that there are only one or two major updrafts. As a result all the clouds live and die exactly in phase so that the total cloud cover makes unreal large fluctuations. Apparently a 2.5-km domain is too small to contain a large enough steady-state cloud ensemble. That the fluctuations do not decrease strongly if we enlarge the domain further from 5 to 10 km is a sign that the cloud ensemble of the 5-km domain is already quite sufficient to describe the cloud dynamics representative for an area that can be, in principle, orders of magnitude larger than the computational domain. The analyses done in the next

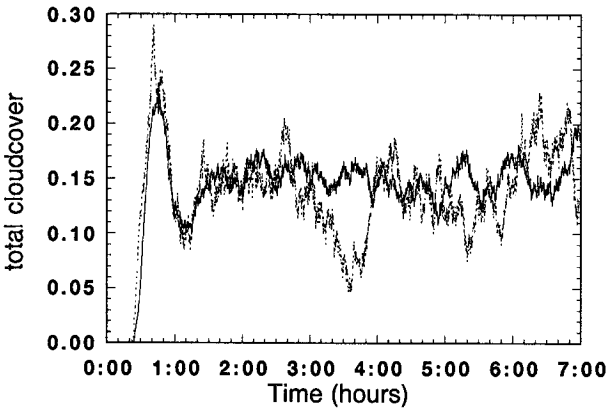

FIG. 5. Total cloud cover as a function of time for a 2.5 × 2.5 km^2 domain (broken line) and 5 × 5 km^2 domain (full line). Note the reduction of the fluctuations in the larger domain due to a larger cloud ensemble.

section will therefore be based on simulations on a 5-km domain.

4. Turbulent flux parameterizations

A basic assumption in many cumulus convection schemes is that vertical turbulent transport can be described in terms of cumulus updrafts and compensating environmental subsidence. To make this notion more precise let us make a decomposition into two parts: an active cloudy part and passive environmental part. The turbulent flux of an arbitrary field χ can then be divided into three terms:

$$\overline{(w'\chi')} = a\overline{w'\chi'}^{c} + (1-a)\overline{w'\chi'}^{e} + a(1-a)(w_c - w_e)(\chi_c - \chi_e), \quad (4.1)$$

where a is the fraction of the active cloudy part and the subscripts c and e label, active cloud and passive environmental averages. The overbar indexed c (e) denotes a cloud (environmental) average of the fluctuations with respect to the cloud (environmental) average. The first term, the in-cloud turbulence, describes the correlated fluctuations *within* the clouds; the second term, the environmental turbulence, describes correlated fluctuations *within* the environment; while the third term, the organized turbulence term, describes the contribution due to average organized updrafts and compensating subsidence in the environment. Note that in (4.1) no approximations are involved. In convection parameterization schemes it is usually assumed that the organized turbulence term is dominant so that

$$\overline{(w'\chi')} = a(1-a)(w_c - w_e)(\chi_c - \chi_e) = a(w_c - \bar{w})(\chi_c - \chi_e) \equiv \frac{M}{\rho}(\chi_c - \chi_e), \quad (4.2)$$

thereby making the approximation

$$a\overline{w'\chi'}^{c}, (1-a)\overline{w'\chi'}^{e} \ll a(1-a)(w_c - w_e)(\chi_c - \chi_e). \quad (4.3)$$

In the last step of (4.2) we defined a convective mass flux M, which is a measure for vertical mass transport. Although the approximation (4.2) is widely used, the validity of (4.3) is hardly discussed in the literature. In some cloud models (Hanson 1981), it is assumed that the first term of the right-hand side of (4.1) should also be included.

Using the LES model, we can determine all the three terms of the right-hand side of (4.1). Hence, the quality of the approximation (4.2) can easily be checked. In order to do so we have to specify how the active cloudy part is defined exactly. Since the literature is not clear at this point, we have tried three different decompositions. The first one, the *cloud* decomposition, defines the active cloudy part simply to be all the grid points in the model with a nonzero liquid water content. More restrictive is the *updraft* decomposition, which defines the active cloud part to be all the points that contain liquid water *and* that have a positive vertical velocity. The most restrictive case is the *core* decomposition in which the active cloudy part consists of all the points that contain liquid water, have a positive vertical velocity, and are also positive buoyant.

In order to check whether cloud downdrafts also play an active role, we consider a fourth possible decomposition into *three* parts instead of into two: cloud updrafts, cloud downdrafts, and environment. In that case, if we estimate the turbulent flux by only the organized turbulence term, we readily find

$$\overline{w'\chi'} \approx a_u(w_u - \bar{w})(\chi_u - \bar{\chi}) + a_d(w_d - \bar{w})(\chi_d - \bar{\chi}) + (1 - a_u - a_d)(w_e - \bar{w})(\chi_e - \bar{\chi}), \quad (4.4)$$

where the subscript d denotes cloud downdraft properties and the subscript u denotes cloud updraft properties. Approximation (4.4) has been proposed by Tiedtke (1989) for the deep convection part of his mass flux scheme. The advantage of such a decomposition over a cloud decomposition (4.1) is to be expected in cases where the convective mass flux of the cloud downdrafts becomes comparable with the cloud updraft mass flux.

We have verified the turbulent flux parameterizations (4.2) and (4.4) for the conserved variables θ_l and q_t and for the nonconserved variables θ and q_l. This has been done by calculating at each time step for each decomposition and for all four variables the left-hand side and the right-hand side of (4.2) and (4.4). Next, we have averaged the flux profiles over the last 4 hours. Such a time average is allowed if the cloud ensemble is in an acceptable stationary state. To test the quality of the stationary state we first calculated 1-h averaged

flux profiles. Since the 1-h-averaged profiles during the last 4-h period were rather identical we concluded that the cloud ensemble was in an acceptable steady state during that period so that an ensemble averaging in time was indeed allowed.

The results for the four turbulent flux approximations are plotted in Figs. 6a–d and compared with the total fluxes as computed directly by the LES model. All four flux decompositions for θ_l, q_t, and q_l give qualitatively reasonable results but systematically underestimate the model fluxes. The results for the potential temperature θ, however, are worse. Only the core decomposition gives qualitatively the correct shape but underestimates this flux by a factor of 2. The other flux decompositions of θ, however, do not even give the right sign. Overall, we can conclude that the fluxes of the conserved variables θ_l and q_t are best described by the updraft decomposition, while the core decomposition gives the best results for the nonconserved variables θ and q_l. The cloud decomposition gives systematically the worst results and should be disregarded. The decomposition (4.4) into three parts does not substantially improve the updraft decomposition. This follows from the fact that in the present shallow convection case the downdraft mass flux is neglectable compared with the updraft mass flux.

Apparently, approximation (4.3) does not hold in general. In order to see whether it is the cloud turbulent flux or the environmental turbulent flux that is responsible for the observed discrepancies we have plotted in Figs. 7a–d all the terms of (4.1). This has been done only for the core decomposition for the variables $\chi = \theta_l, \theta, q_t$, and q_l. From these figures we can conclude that the discrepancies are mainly due to $\overline{w'\chi'}^c$, with the restriction of the areas near cloud base and cloud top where $\overline{w'\chi'}^e$ becomes the dominant term for explaining the discrepancy.

Most of the above-reported results can be understood easily on a qualitative basis. First, that $\overline{w'\chi'}^c$ can give a considerable contribution is because the variability of w and χ is strongly correlated within clouds. Toward the core of the clouds there is in general more condensation and less detrainment/entrainment, giving rise to stronger updrafts, more liquid water, a higher potential temperature, and a lower liquid potential temperature. Clearly, these effects cannot be taken into account by (4.2) and give rise to $\overline{w'\theta_l'}^c < 0$ and $\overline{w'\theta'}^c$, $\overline{w'q_t'}^c$, and $\overline{w'q_l'}^c > 0$, qualitatively in agreement with the observed fluxes. Second, $\overline{w'\chi'}^e$ gives (at least for the core decomposition) significant contributions near cloud base because the dry boundary layer turbulence slightly penetrates into the cloud layer. Near the cloud top $\overline{w'\chi'}^e$ becomes more important due to the vanishing core and resulting detrainment of cloud core air with the above-described correlations into the environment.

The reason that the approximation (4.2) is much worse for θ than for the other three fields is due to the fact that the average cloud temperature excess is very small. As a result the contribution of the third term of (4.1) is much smaller than in the case of θ_l. On the other hand, correlation between θ and w within clouds is evidently stronger than between θ_l and w, resulting in a higher $\overline{w'\theta'}^c$. As a result $\overline{w'\theta'}^c$ is in most decompositions the *dominant* term, while in the case of the core decomposition it is of the same magnitude as the approximation (4.2).

These outcomes are somewhat in contradiction with an LES study of the Puerto Rico case by Beniston and Sommeria (1981), who found a better agreement between model turbulent fluxes of θ_l and q_t and the parameterization (4.2) using the cloud decomposition. An important difference with the present case, however, is the fact that they used a much smaller horizontal domain of 2×2 km^2. We therefore repeated our experiment on such a small domain and indeed found a significant improvement of all four parameterizations (4.2). As already discussed in section 2 there can exist only one or two major updrafts on such a small domain so that the life cycles are mutual in phase. Clearly, an approximation like (4.2) is expected to work better for such an unreal "in phase" cloud ensemble.

The above results have important consequences with respect to shallow convection parameterizations. Suppose we are dealing with a parameterization scheme that can diagnose perfectly the right cloud-updraft and cloud-core fields. Even in such an ideal case, when using the updraft decomposition (4.2), we would underestimate the fluxes of q_t, q_l, and θ_l by 10% to 40%, while the θ flux approximation would be completely wrong. Using (4.2) with the core decomposition would give at least the proper shape of the θ flux but would underestimate the θ flux by a factor of 2. In conclusion, when parameterizing turbulent fluxes using (4.2) in combination with a (hypothetical) perfect cloud model using the nonconserved variables q_v, q_l, and θ, the best one can do is to use the core decomposition. By using a proper enhancement factor one can obtain then reasonable results for the various turbulent fluxes.

Let us proceed investigating the organized turbulence term (4.2) in some more detail. This term is essentially the product of the convective mass flux M and an average cloud excess value of the field χ under consideration. The convective mass flux determines the intensity of the convection and is a key parameter to be determined in many convection parameterization cloud schemes.

In Fig. 8 we have plotted the cloud cover and the vertical velocity excess $w_c - \bar{w}$, the components that build up the convective mass flux M. Results for both the core and the updraft are shown. The cloud cover is strongly decreasing with height, indicating that only few clouds actually reach the inversion layer. The cloud cover of the core is roughly 60% of the updraft cloud cover. Apparently, 40% of the clouds are nonbuoyant forced clouds (Stull 1985). The in-cloud vertical ve-

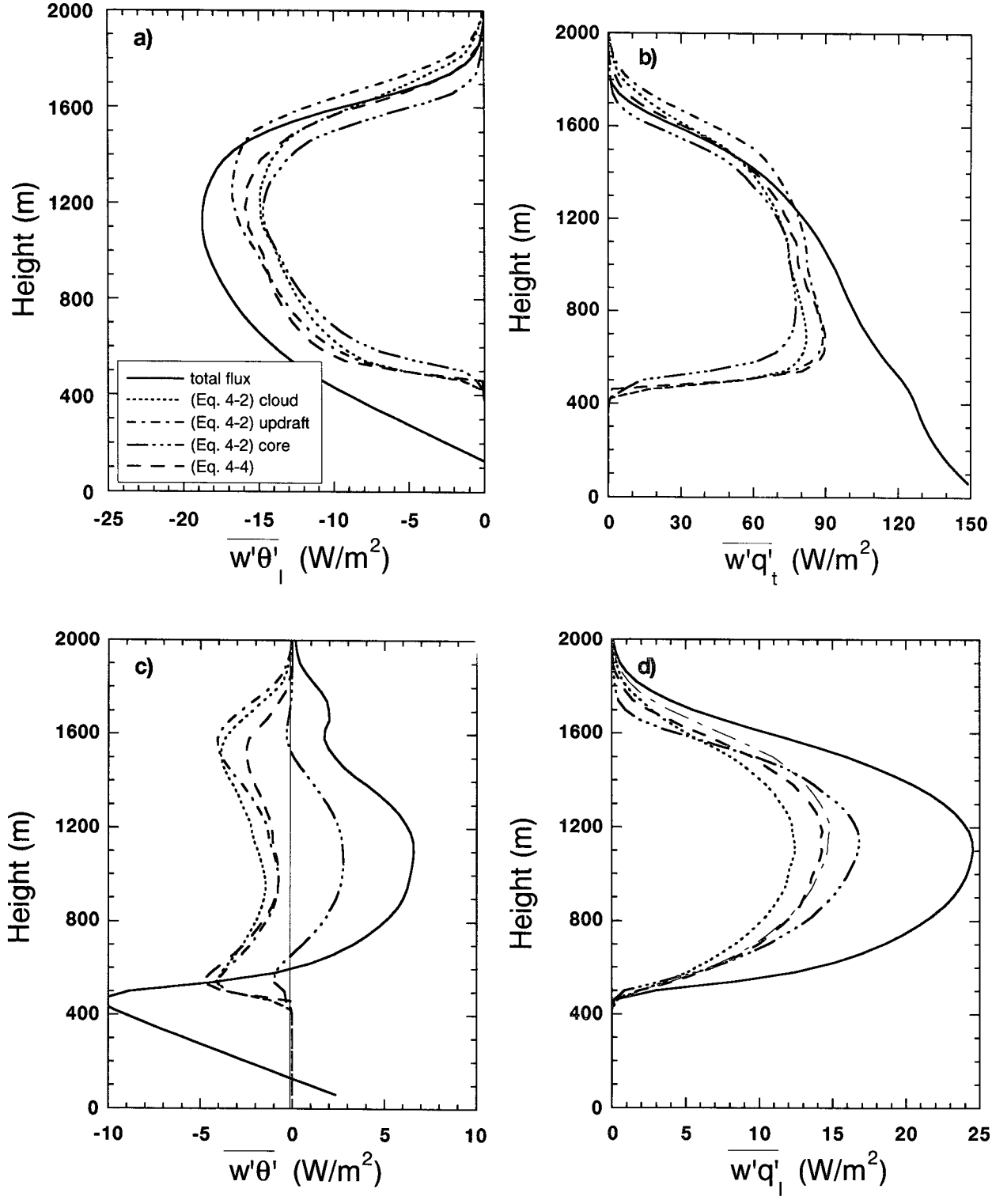

FIG. 6. The various turbulent flux decomposition approximations as given by (4.2) and (4.4) for θ_l (a), q_t (b), θ (c), and q_l (d), averaged over the last 4 h.

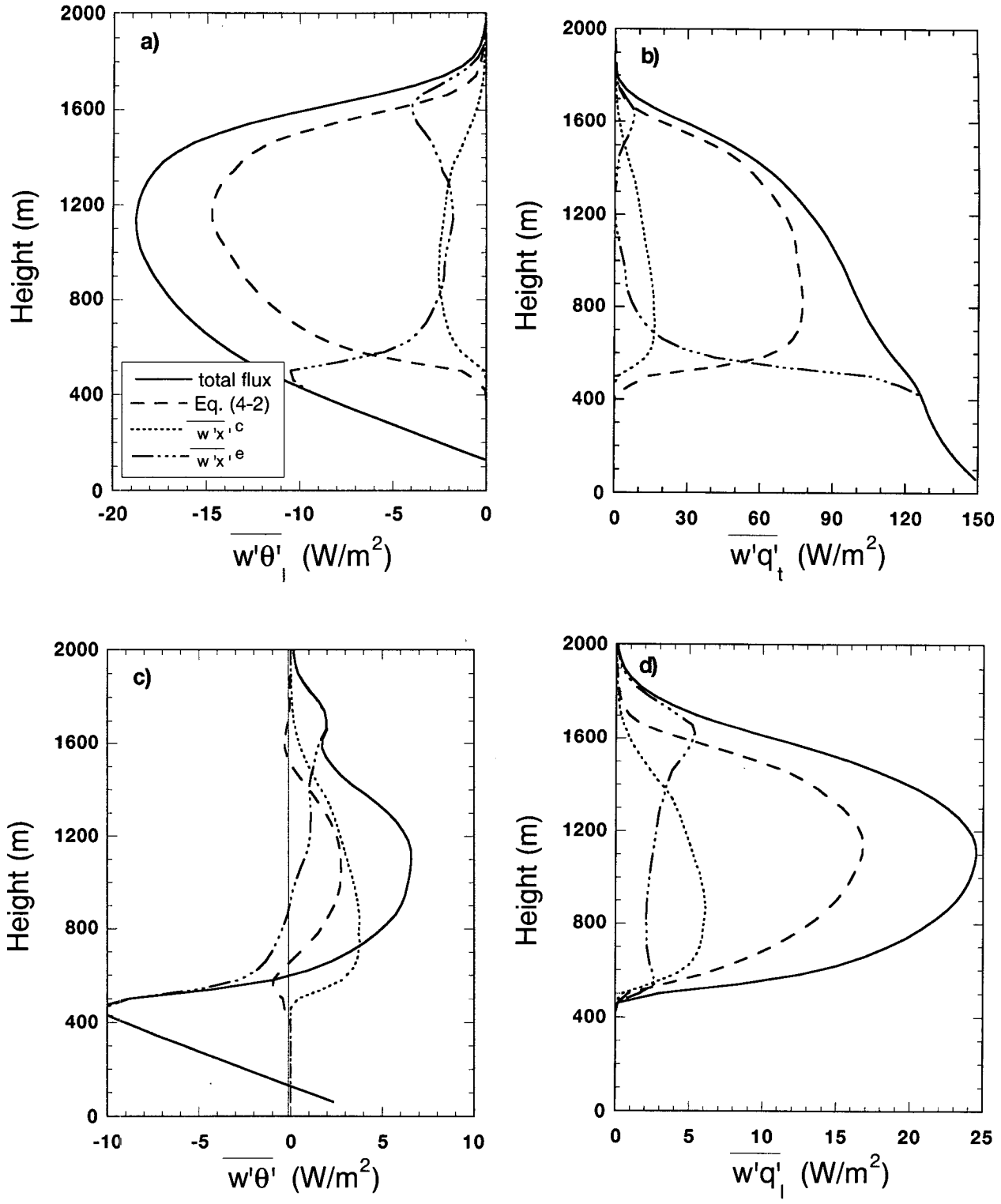

FIG. 7. The three contributions to the turbulent flux as given by (4.1) averaged over the last 4 h in the case of the core decomposition for θ_l (a), q_t (b), θ (c), and q_l (d).

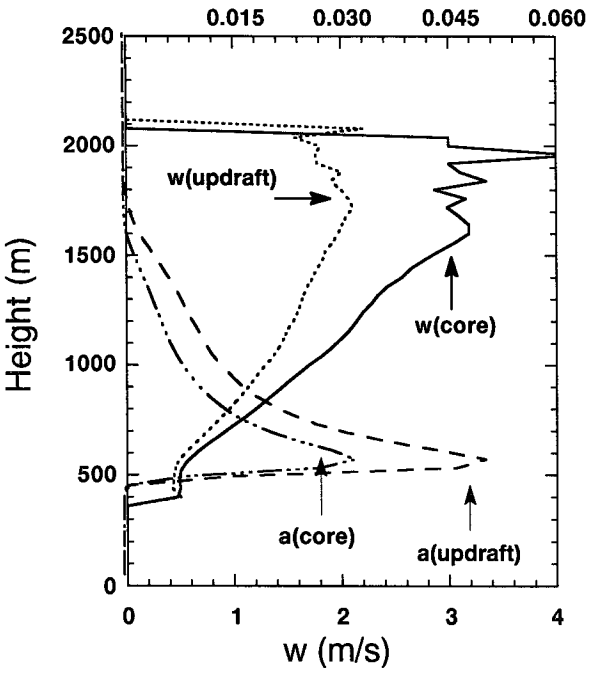

FIG. 8. Cloud cover and vertical velocity excess for the cloud updraft and the cloud core as a function of height averaged over the last 4 h of the simulation. The product of these two quantities essentially build up the convective mass flux.

locity is increasing in the conditionally unstable layer and is damped strongly in the inversion layer. The resulting convective mass flux, displayed in Fig. 9, is monotonically decreasing with height due to the cloud cover profile. In the same figure we show some results of Esbensen (1978), who found the same profile and order of magnitude for the mass flux by applying a cloud model on the BOMEX dataset. As a consequence, the detrainment, the outflow of mass from clouds, will be systematically larger than the entrainment, the inflow from mass into clouds, as will be discussed in detail in the next section. The fact that the cloud cover is a nontrivial function of height makes it difficult to construct a physically sound parameterization of the mass flux. While the cloud vertical velocity can be estimated from a buoyancy equation, the cloud cover is not so easy to estimate. In some cloud models it is simply assumed that the cloud cover does not change with height (Hanson 1981). Clearly, such an approach cannot work in the present case.

All the decompositions considered so far are based on the presence of clouds. Recently, another decomposition has been proposed (Moeng et al. 1992; Randall et al. 1992), based only on the sign of the vertical velocity. The turbulent flux of a field χ can then be approximated as

$$(\overline{w'\chi'}) \sim a(w_{up} - \bar{w})(\chi_{up} - \chi_{do}), \qquad (4.5)$$

where the index up (do) refers to an average over all the points with a positive (negative) velocity. Such a decomposition works well for clear and stratus-topped boundary layers. The advantage of such a decomposition is that it can also be used in the cloud-free boundary layer, which would open the way to a unified mass flux parameterization for both the boundary layer and the convective clouds on top. We have checked the quality of approximation (4.5). Unfortunately, the results were not very positive: the estimated fluxes in the cloud layer using (4.5) were one order of magnitude smaller than the total turbulent fluxes. The reason for this follows from the fact that $\chi_{up} - \chi_{do}$ is too small. Also, the introduction of a third "environmental" domain in which the vertical velocity is nearly zero as suggested by Greenhut and Khalsa (1987) did not improve the results in the cloud layer.

5. Entrainment and detrainment

a. General

Entrainment of dry air into cumulus clouds and detrainment of cloudy air into the environment affects the dynamics of clouds and their interaction with the environment in a major way. For cloud models used in cumulus parameterizations it is crucial to have a realistic description of the overall mass exchange between a cloud ensemble and the environment.

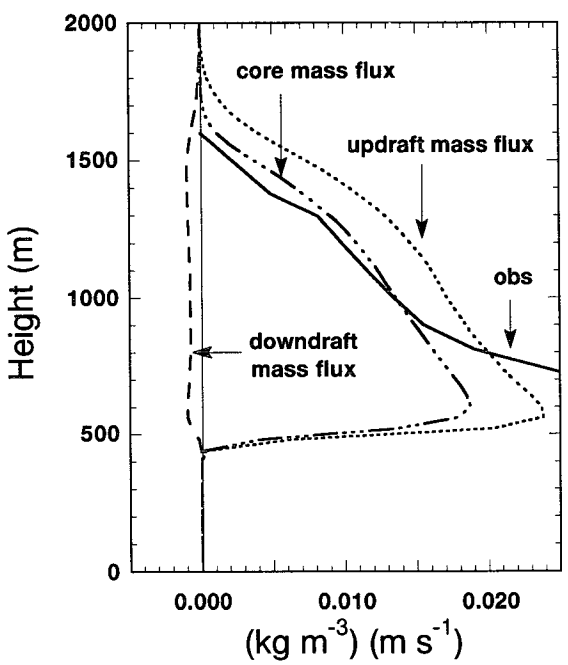

FIG. 9. The convective mass flux M of the cloud updraft, the cloud downdraft, and the cloud core. The thick line refers to results of Esbensen (1978) diagnosed from the BOMEX data using a cloud model.

The simplest approach is to assume an ensemble of identical steady-state clouds, all reaching from the same base to the same top height. Inflow of air (entrainment) mainly occurs at cloud base and outflow (detrainment) of air mainly at the cloud top. Within such a model cloud temperature can be found using a moist adiabat. Specific humidity and liquid water in the cloud can be found by lifting a saturated parcel from the cloud base following the moist adiabat. If finally the mass flux at cloud base is specified then the turbulent transport due to cloud updrafts can be easily calculated using (4.2). The physical picture emerging from such a description is one where heat and moisture is injected at cloud base, transported without leakages through the cloud channels, and finally massively detrained at cloud top and slowly mixed downward in the environment by the compensating subsidence.

Unfortunately, life is not so simple as described above. First, only the cloud ensemble as a whole is in a steady state. The individual clouds all have their own individual life cycle. Assuming the current picture (Blyth 1993) that entrainment of a single growing cloud is mainly occurring at the ascending cloud top, it is clear that, even if all clouds reach the same cloud-top height z_t, the entrainment rate of the cloud ensemble is nonzero within the whole cloud layer. Second, a cloud ensemble usually exhibits a wide spread in the cloud-top height distribution. Therefore, when assuming the simplified picture that detrainment of an individual cloud only occurs in its adult state at cloud top, we also expect for the detrainment rate a nonzero contribution at all heights within the whole cloud layer. As a result, when parameterizing convection using a bulk cloud model one has to take lateral entrainment and detrainment into account for the whole cloud layer to mimic the presence of a nonuniform cloud ensemble.

Little progress has been achieved in the theoretical description over the last 30 years [see Blyth (1993) for a recent review]. Results for entrainment rates are mainly obtained for single plumes and thermals. In parameterization studies not much effort has been made to translate these results to cloud ensembles. Notable exceptions are spectral convective cloud parameterizations such as the scheme of Arakawa and Schubert (1974).

b. *Determination of the entrainment and detrainment*

During the large-eddy simulation we carefully monitored both cloud and environment dynamics. We are therefore in a situation where we can accurately calculate the entrainment and detrainment rates of the simulated cloud ensemble. In order to do so we have to decompose the prognostic equations (2.2)–(2.4) of the conserved variables $\chi = \theta_l, q_t$ into an active cloudy part and an environmental part using the exact decomposition formula of the turbulent fluxes (4.1), resulting in

$$\rho \frac{\partial a\chi_c}{\partial t} = -\frac{\partial M_c\chi_c}{\partial z} + E\chi_e - D\chi_c - \frac{\partial \rho a\overline{w'\chi'}^c}{\partial z} + a\rho\left(\frac{\partial \bar{\chi}}{\partial t}\right)_{\text{forcing}}$$

$$\rho \frac{\partial (1-a)\chi_c}{\partial t} = +\frac{\partial M_c\chi_e}{\partial z} - E\chi_e + D\chi_c - \frac{\partial \rho(1-a)\overline{w'\chi'}^e}{\partial z} + \rho(1-a)\left(\frac{\partial \bar{\chi}}{\partial t}\right)_{\text{forcing}}, \quad (5.1)$$

where an entrainment rate E and a detrainment rate D are introduced to describe the mass exchange between cloud and environment. Note that the original prognostic equation (2.2) can be easily recovered by adding the cloudy and environmental part and using the flux decomposition (4.1). In order to obtain separate equations for E and D, we also use the continuity equation within the quasi-Boussinesq approximation for the active cloudy part (Arakawa and Schubert 1974):

$$\rho \frac{\partial a}{\partial t} = -\frac{\partial M_c}{\partial z} + E - D. \quad (5.2)$$

Expressions for the entrainment and detrainment can now easily be found by eliminating $\partial a/\partial t$ in (5.1) using (5.2):

$$E(\chi_e - \chi_c) = M_c \frac{\partial \chi_c}{\partial z} + \frac{\partial \rho a\overline{w'\chi'}^c}{\partial z} + \rho a \frac{\partial \chi_c}{\partial t} - a\rho\left(\frac{\partial \bar{\chi}}{\partial t}\right)_{\text{forcing}} \quad (5.3a)$$

$$D(\chi_e - \chi_c) = M_c \frac{\partial \chi_e}{\partial z} - \frac{\partial \rho(1-a)\overline{w'\chi'}^e}{\partial z} + \rho(1-a)\frac{\partial \chi_c}{\partial t} + \rho(1-a)\left(\frac{\partial \bar{\chi}}{\partial t}\right)_{\text{forcing}}. \quad (5.3b)$$

During the LES run we have determined at each time step all the terms on the right-hand side of (5.3). All these terms are integrated over the last 4 hours of the simulation. Because of the steady state the time derivatives are negligible. Also, the forcing term in (5.3a) is very small since $a \ll 1$. Hence, the entrainment rate as given by (5.3a) is mainly determined by the average cloud excess values $(\chi_c - \chi_e)$ and the turbulent fluxes. We have determined E as a residual from the time-averaged terms of Eq. (5.3a), both for the updraft decomposition and the core decomposition. As a consistency check we did all the calculations both for θ_l and q_t. As expected, the obtained rates were exactly the same for both variables. As shown in Fig. 10a, the entrainment rate is for both decompositions monotonically decreasing from cloud base to cloud top. The entrainment rate into the core is systematically smaller than the entrainment rate into the updraft. This is due

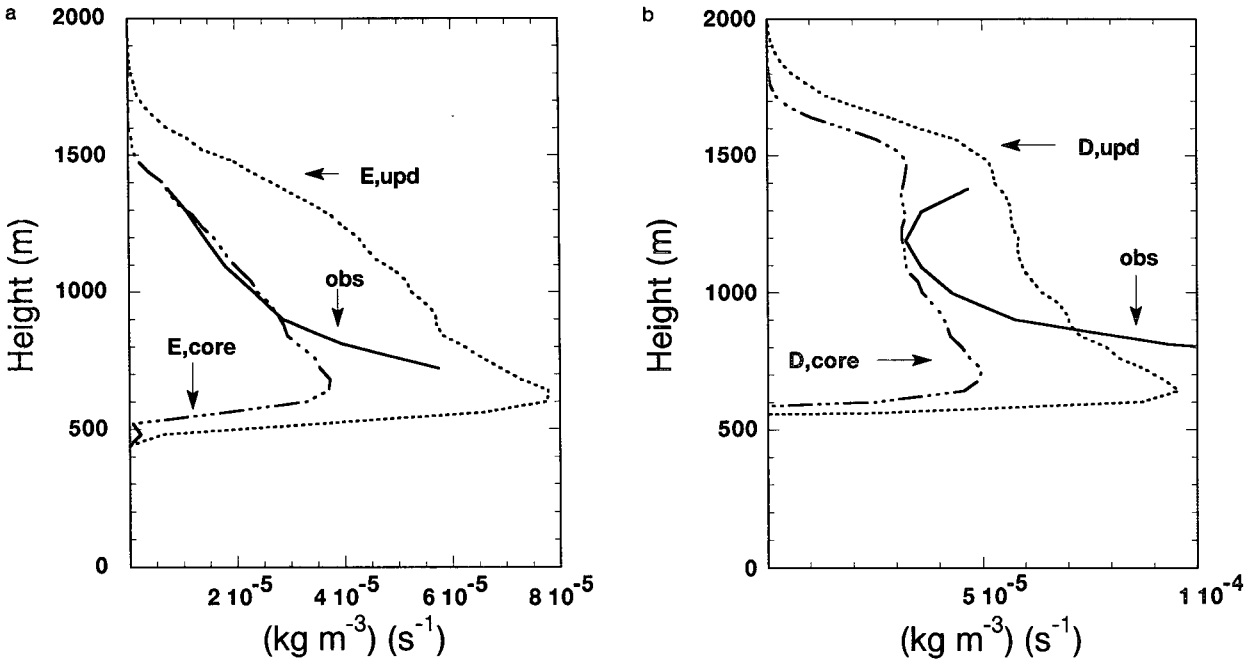

FIG. 10. Entrainment rate E (a) and detrainment rate D (b) for both the core and the updraft decomposition averaged over the last 4 h. The thick line refers to results of Esbensen (1978) based on the BOMEX dataset.

to the fact that the core is mostly contained within the updraft. Hence, the entrainment rate into the core is not likely to exceed the entrainment rate into the updraft. Note further that there is good agreement with results of Esbensen (1978), who has applied a cloud model to determine E and D directly from the BOMEX dataset.

A similar formula like (5.3) for the entrainment and detrainment rate has been obtained by Hanson (1981). However, the rates in that paper are normalized with the cloud cover, which is assumed to be constant with height so that the cloud cover could be eliminated from the equations. From the present simulation we know that this is quite an erroneous assumption. In fact, the height dependence of the mass flux is largely determined by the height dependence of the cloud cover. In other papers (Betts 1975), Eq. (5.3) is presented without the second term of the right-hand side. For the conserved variables θ_l and q_t this term can be neglected in the middle of the cloud layer. However, near cloud base and cloud top it is of the same order as the other terms and cannot be neglected. For instance ignoring this term would give an erroneous increase of the entrainment rate near cloud base of 30%.

The detrainment rate can be determined in two ways. One method is to calculate the rate using (5.3b), similar to the entrainment rate computation. Another way is using the continuity equation (5.2) in combination with the already obtained results for the entrainment rate. We have done both calculations and found identical results. Results are shown in Fig. 10b together with the results of Esbensen (1978). Like in the case with entrainment we also find here exactly the same detrainment rates for θ_l and q_t and higher rates for the updraft decomposition than for the core decomposition.

Comparing entrainment and detrainment rates, we see that the detrainment rate is systematically higher than the entrainment rate. This implies the following cloud dynamical picture. At cloud base the mass flux is fed from the boundary layer below. This mass flux is decreasing with height because there is a net lateral leakage of mass from the clouds into the environment since the detrainment rate is systematically larger than the entrainment rate. The main reason for this is the fact that the cloud cover is monotonically decreasing with height.

c. *Comparison of the results with entrainment parameterizations*

Entrainment rates used in cumulus parameterization schemes all are based on studies of single thermals and plumes. These studies (Squires and Turner 1962; Simpson and Wiggert 1969; Simpson 1971) suggest that the fractional entrainment rate ϵ, that is, the ratio of the entrainment rate E and the convective mass flux M, is proportional to the inverse radius of the thermal:

$$\epsilon \equiv \frac{E}{M_c} \approx \frac{\eta}{R}, \tag{5.4}$$

where the dimensionless proportionality constant η is usually chosen to be $\eta = 0.2$. This result is often used in cumulus parameterizations to estimate the entrain-

ment rate of a cloud ensemble where R is chosen to be a *typical* cloud radius. In the ECMWF mass flux scheme (Tiedtke 1989) a fixed fractional entrainment rate for shallow convection of $\epsilon = 3 \times 10^{-4}$ m^{-1} is used. The operational mass flux scheme at the U.K. Meteorological Office (Gregory and Rowntree 1990) assumes a value of $\epsilon = 4 \times 10^{-4}$ m^{-1} for shallow convection.

The fractional entrainment rate ϵ has been determined from LES output using the definition (5.4). Results are shown in Fig. 11 for both the core and the updraft decomposition. In the lower cloud layers between 500 and 1250 m we find for the fractional entrainment rate the following typical values:

$$\epsilon \approx 3 \times 10^{-3}\ \text{m}^{-1}, \quad \text{for the updraft}$$
$$\epsilon \approx 1.5 \sim 2.0 \times 10^{-3}\ \text{m}^{-1}, \quad \text{for the core.} \qquad (5.5)$$

These value are almost one order of magnitude higher than the values used in the above-cited schemes. Clearly something, somewhere, must be wrong. Let us explore the various possibilities for this inconsistency.

First, the simulation results for the fractional entrainment could be wrong by an order of magnitude. This seems unlikely since all the features of the simulated cloud ensemble compare quite well with the experimental data. The diabatic cooling and moistening of the cloud field as simulated corresponds well with the BOMEX dataset. Moreover, the entrainment rate and convective mass flux as computed by the model correspond well with cloud model results of Esbensen (1978), based directly on the BOMEX dataset.

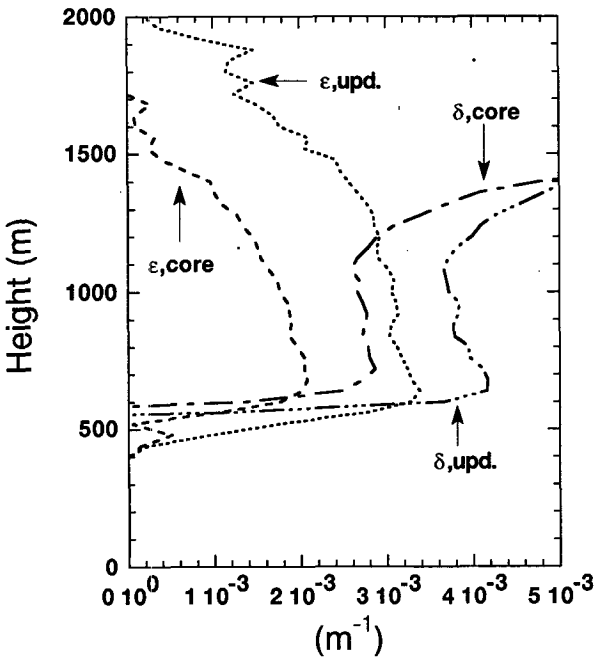

FIG. 11. Fractional entrainment ϵ and detrainment δ rate for both the core and the updraft decomposition averaged over the last 4 h.

Second, one can doubt the validity of (5.4). In a recent review on entrainment research of over 30 years, this formula is discussed (Blyth 1993). Indeed, an uncertainty of a factor of 2 in the proportionality factor η seems to exist—not enough, however, to explain the observed discrepancy.

Probably the most likely reason for the discrepancy is the assumption that *one* typical cloud can give a good estimate for the entrainment rate for the whole ensemble. This might be a good estimate for a rather uniform cloud distribution, but if the ensemble consists of a broad distribution of different cloud types this may give rise to huge errors. Instead, in such a case it is better, à la Arakawa and Schubert (1974), to divide the ensemble into subsets of clouds $\{z_t\}$ that reach the same cloud-top height z_t. Assuming that clouds belonging to a subset $\{z_t\}$ have identical radii $R(z, z_t)$, one can write down an expression that relates the total fractional entrainment rate of the cloud ensemble in terms of the fractional entrainment rates of individual clouds that can be described by (5.4). To do so, let us introduce $m(z, z_t)$ and $\epsilon(z, z_t)$ to be, respectively, the mass flux and the fractional entrainment rate at z of that cloud subset $\{z_t\}$ that reaches a maximum cloud-top height z_t. One then readily finds for the fractional entrainment rate of the ensemble:

$$\langle \epsilon(z) \rangle_{\text{cloud ensemble}} = \frac{\int_z^\infty \epsilon(z, z_t) m(z, z_t) dz_t}{\int_z^\infty m(z, z_t) dz_t}. \qquad (5.6)$$

Equation (5.6) illustrates that $\langle \epsilon(z) \rangle$ is related to $\epsilon(z, z_t) \sim \eta / R(z, z_t)$ by some sort of weighted average, where the weight of a given subset is proportional to the magnitude of the mass flux of that specific subset. A spectral cloud analysis of the BOMEX dataset (Nitta 1975) shows indeed a broad distribution of cloud tops, where in fact the mass flux of the subset of small clouds, having a radius of 100 m, is dominant. The entrainment rate of this dominant subset is according to (5.4) 2×10^{-3} s^{-1}, close to the value simulated by the model. With the present resolution of 125 m, however, it is not possible to resolve such small clouds. In order to explore the aforementioned explanation it is necessary to do simulations with a higher horizontal resolution and to perform spectral cloud analyses.

d. *Comparison of the results with detrainment parameterizations*

In the ECMWF shallow convection scheme (Tiedtke 1989) a fractional detrainment rate $\delta \equiv D/M$ is introduced and defined to be equal to the fractional entrainment rate ϵ, while in the scheme of the UKMO model (Gregory and Rowntree 1990) δ is chosen to be one-

third of ϵ. As a result, the bulk mass flux in the above schemes is constant or even increasing with height. Therefore, at the zero buoyancy level in the inversion layer, there has to be a massive detrainment [called *organized* detrainment by Tiedtke (1989) and *forced* detrainment by Gregory and Rowntree (1990), which is much larger than the detrainment within the cloud layer. While such a picture might be correct for deep convection it is not valid for shallow convection. In the present case detrainment is systematically *larger* than the entrainment rate so that the mass flux is decreasing with height. As a result, there is no massive detrainment in the inversion layer.

Qualitatively we can conclude that in the case of shallow convection one has to parameterize δ to be larger than ϵ, resulting in a quite different but more realistic dynamics. Quantitatively the same criticism applies as in the case of entrainment: the values of δ used in the aforementioned parameterization schemes are more than an order of magnitude too small compared with the results obtained from the simulation. From Fig. 11 we find a rather constant fractional detrainment rate in the lower cloud layer of

$$\delta \approx 4 \times 10^{-3}\ \mathrm{m}^{-1}, \quad \text{for the updraft}$$
$$\delta \approx 3 \times 10^{-3}\ \mathrm{m}^{-1}, \quad \text{for the core,} \qquad (5.7)$$

which has to be compared with $\delta = 3 \times 10^{-4}\ \mathrm{m}^{-1}$ (Tiedtke 1989) and $\delta = 1.3 \times 10^{-4}\ \mathrm{m}^{-1}$ (Gregory and Rowntree 1990), values used in present parameterization schemes.

6. Conclusions and perspectives

Trade wind cumuli such as observed during BOMEX have been simulated by an LES model for a period of 7 hours. From these simulations variables often used in parameterizations have been derived such as turbulent fluxes, mass fluxes, entrainment, and detrainment rates. Since the simulations were done under realistic steady-state conditions, time averaging of these variables could be performed, thereby reducing unwanted fluctuations and sample dependencies.

For the turbulent fluxes it has been investigated how well a turbulent flux can be approximated by a single bulk updraft and a compensating subsidence as proposed by Betts (1975). Such an approximation gives the best results for the core decomposition. Even when using this decomposition, however, such an approximation underestimates the turbulent fluxes, especially for the potential temperature, due to the fact that the in-cloud and environmental turbulent terms are neglected. Since the shape of the in-cloud turbulence profile is similar to the one of the organized turbulent term, this can easily be taken into account by introducing an appropriate enhancement factor. The environmental turbulent flux term near cloud base can in principle be calculated by a dry boundary layer scheme that accounts properly for the dry convection (Holtslag and Boville 1993). Also, flux decompositions that are only based on updrafts and downdrafts have been investigated. Such decompositions are potentially interesting since they also give estimates for the dry boundary layer below. Unfortunately, the present results indicate that these decompositions give poor results, especially in the cloud layer.

For the fractional entrainment and detrainment rates we have obtained values that are one order of magnitude larger than values used in operational shallow convection parameterization schemes. As a consequence the modeled shallow convective clouds in such schemes will be too high, so that the vertical mixing of heat and moisture will be too deep. Another important outcome of the simulation is that the detrainment rate is systematically larger than the entrainment rate, resulting in a net outflow of mass all the way from cloud base to cloud top. As a result, the mass flux is a decreasing function of height. This provides quite a different picture than promoted in most parameterization schemes, where it is assumed that mass flux can flow without losses from cloud base to cloud top, where it massively detrains. These features are probably quite typical for shallow convection in general, mainly due to fact that there are many small clouds and relatively few big clouds reaching the inversion. In fact when the cloud size distribution is known and if a well-defined relationship exists between vertical extent and the radius of a cloud, one can obtain analytical results for the fractional entrainment and detrainment rates by solving integrals like (5.6).

Acknowledgments. It is a pleasure to thank A. A. M. Holtslag, M. Tiedtke, and A. P. van Ulden for interesting discussions. The authors also would like to thank S. Esbensen and two anonymous referees for useful comments and suggestions on an earlier version of the paper. J. W. M. Cuijpers acknowledges financial support of the Netherlands organization for scientific research (NWO) under Contract 752-365-031.

REFERENCES

Albrecht, B. A., A. K. Betts, W. H. Schubert, and S. K. Cox, 1979: A model of the structure of the trade-wind boundary layer: Part I. Theoretical formulation and sensitivity tests. *J. Atmos. Sci.*, **36,** 73–89.

Arakawa, A., and H. Schubert, 1974: Interaction of a cumulus cloud ensemble with the large-scale environment. Part I: Theoretical formulation and sensitivity tests. *J. Atmos. Sci.*, **31,** 674–701.

Augstein, E., H. Riehl, F. Ostapoff, and V. Wagner, 1973: Mass and energy transports in an undisturbed trade-wind flow. *Mon. Wea. Rev.*, **101,** 101–111.

BOMEX Center for Experiment Design and Data Analysis, 1975a: *BOMEX Rawinsonde Atlas,* 146 pp.

——, 1975b: *BOMEX Period III Atlas of Low-Level Atmospheric Data,* 56 pp.

Beniston, M. G., and G. Sommeria, 1981: Use of a detailed planetary boundary layer model for parameterization purposes. *J. Atmos. Sci.*, **38,** 780–797.

Betts, A. K., 1975: Parametric interpretation of trade-wind cumulus budget studies. *J. Atmos. Sci.*, **32,** 1934–1945.

Blyth, A. M., 1993: Entrainment in cumulus clouds. *J. Appl. Meteor.*, **32,** 626–641.

Bougeault, Ph., 1981: Modeling the trade-wind cumulus boundary layer. Part I: Testing the ensemble cloud relations against numerical data. *J. Atmos. Sci.*, **38,** 2414–2439.

Cuijpers, J. W. M., 1994: Large eddy simulation of cumulus convection. Ph.D. thesis, Delft University of Technology, the Netherlands, 158 pp.

——, and P. G. Duynkerke, 1993: Large eddy simulation of trade-wind cumulus clouds. *J. Atmos. Sci.*, **50,** 3894–3908.

Deardorff, J. W., 1973: Three-dimensional numerical modeling of the planetary boundary layer. *Workshop on Micrometeorology,* D. A. Haugen, Ed., Amer. Meteor. Soc., 271–311.

Dyer, A. J., 1974: A review of flux-profile relationships. *Bound.-Layer Meteor.*, **7,** 363–372.

Esbensen, S., 1978: Bulk thermodynamic effects and properties of small tropical cumuli. *J. Atmos. Sci.*, **35,** 826–837.

Greenhut, G. K., and S. J. S. Khalsa, 1987: Convective elements in the marine atmospheric boundary layer. Part I: Conditional sample statistics. *J. Climate Appl. Meteor.*, **26,** 813–822.

Gregory, D., and P. R. Rowntree, 1990: A mass flux scheme with representation of cloud ensemble characteristics and stability-dependent closure. *Mon. Wea. Rev.*, **118,** 1483–1506.

Hanson, H. P., 1981: On mixing by trade-wind cumuli. *J. Atmos. Sci.*, **38,** 1003–1014.

Holland, J. Z., 1972: Comparative evaluation of some BOMEX measurements of sea surface evaporation, energy flux, and stress. *J. Phys. Oceanogr.*, **2,** 476–486.

——, and E. M. Rasmusson, 1973: Measurement of atmospheric mass, energy and momentum budgets over a 500-kilometer square of tropical ocean. *Mon. Wea. Rev.*, **101,** 44–55.

Holtslag, A. A. M., and B. A. Boville, 1993: Local versus nonlocal boundary-layer diffusion in a global climate model. *J. Climate,* **6,** 1825–1842.

Moeng, C.-H., S. Shen, and D. A. Randall, 1992: Physical processes within the nocturnal stratus-topped boundary layer. *J. Atmos. Sci.*, **49,** 2384–2401.

Nicholls, S., M. A. Lemone, and G. Sommeria, 1982: The simulation of a fair weather marine boundary layer in GATE using a three-dimensional model. *Quart. J. Roy. Meteor. Soc.*, **108,** 167–190.

Nitta, T., 1975: Observational determination of cloud mass flux distributions. *J. Atmos. Sci.*, **32,** 73–91.

——, and S. Esbensen, 1974: Heat and moisture budget analyses using BOMEX data. *Mon. Wea. Rev.*, **102,** 17–28.

Paulson, C. A., E. Leavitt, and R. G. Fleagle, 1972: Air–sea transfer of momentum and water determined from profile measurements during BOMEX. *J. Phys. Oceanogr.*, **2,** 487–497.

Peixoto, J. P., and A. H. Oort, 1992: *Physics of Climate.* American Institute of Physics, 520 pp.

Randall, D. A., Q. Shao, and C.-H. Moeng, 1992: A second-order bulk boundary-layer model. *J. Atmos. Sci.*, **49,** 1903–1923.

Roeckner, E., K. Arpe, L. Bengtsson, S. Brinkop, L. Dümenil, E. Kirk, F. Lunkeit, M. Esch, M. Ponater, B. Rockel, R. Sausen, U. Schlese, S. Schubert, and M. Windelband, 1992: Simulation of the present-day climate with the ECHAM model: Impact of model physics and resolution. Max Planck Institute Report No. 93, 173 pp.

Simpson, J., 1971: On cumulus entrainment and one-dimensional models. *J. Atmos. Sci.*, **28,** 449–455.

——, and V. Wiggert, 1969: Models of precipitating cumulus towers. *Mon. Wea. Rev.*, **97,** 471–489.

Sommeria, G., 1976: Three-dimensional simulation of turbulent processes in an undisturbed trade-wind boundary layer. *J. Atmos. Sci.*, **33,** 216–241.

——, and M. A. Lemone, 1978: Direct testing of a three-dimensional model of the planetary boundary layer against experimental data. *J. Atmos. Sci.*, **35,** 25–39.

Squires, P., and J. S. Turner, 1962: An entraining jet model for cumulonimbus updraughts. *Tellus,* **14,** 422–434.

Stull, R. B., 1985: A fair-weather cumulus cloud classification scheme for mixed layer studies. *J. Climate Appl. Meteor.*, **24,** 49–56.

Tiedtke, M., 1989: A comprehensive mass flux scheme for cumulus parameterization in large-scale models. *Mon. Wea. Rev.*, **177,** 1779–1800.

——, W. A. Hackley, and J. Slingo, 1988: Tropical forecasting at ECMWF: The influence of physical parameterization on the mean structure of forecasts and analyses. *Quart. J. Roy. Meteor. Soc.*, **114,** 639–664.

Yanai, M., S. Esbensen, and J.-H. Chu, 1973: Determination of the bulk properties of tropical cloud clusters from large scale heat and moisture budgets. *J. Atmos. Sci.*, **30,** 611–627.